The Arrest and Recession Dynamics of a Deflating Hydraulic Fracture in a Permeable Elastic Medium in a State of Plane Strain

Anthony Peirce[(†)] and Emmanuel Detournay[(⋆)]

(†) Department of Mathematics

The University of British Columbia

Vancouver, BC, Canada V6T 1Z2

peirce@math.ubc.ca

(⋆) Department of Civil, Environmental & Geo-Engineering

University of Minnesota

Minneapolis, MN 55455, USA

August 23, 2022

We investigate the deflation dynamics of a fluid-driven fracture in a permeable elastic medium in a state of plane strain after fluid injection has ceased. Depending on the leak-off characteristics of the porous medium and the volume of injected fluid retained in the fracture at the time of shut-in, the fracture may start to recede almost immediately or continue to propagate

till it arrests when the stress intensity factor drops below the fracture toughness. While occupying the arrest footprint, the fracture continues to deflate while the stress intensity factor decreases due to fluid loss to the porous medium. When the stress intensity factor drops to zero, the fracture starts the process of recession, which continues until it finally collapses. To establish a rigorous numerical scheme to explore the deflation dynamics of plane strain hydraulic fractures, we use recently established vertex and multiscale tip asymptotes for arrested and receding hydraulic fractures [33], including the r-vertex linear tip aperture asymptote $\hat{w} \sim \hat{x}$ for a receding hydraulic fracture and the stationary g-vertex asymptote $\hat{w} \sim \hat{x}^{3/4}$. Numerical experiments demonstrate that the multiscale asymptotes are required in order to achieve solutions that remain smooth through the arrest-recession transition point. In contrast, numerical solutions, obtained by only using vertex solutions to model the arrest and recession, exhibit jump discontinuities through this transition point. However, once the transients from these jump discontinuities have decayed the numerical schemes that use vertex and multiscale asymptotes yield almost identical solutions. A scaling analysis shows the existence of asymptotic power law behaviour for various quantities, such as the arrest time, in terms of two new dimensionless parameters. Finally, numerical solutions explore the dependence on the two dimensionless parameters of the arrest time, the duration of the arrest period, and the duration of the recession phase and confirm their asymptotic power law behaviours.

Key words: Plane Strain, Post Injection Hydraulic Fracture Deflation, Arrest, Recession, Multiscale Tip Asymptotics.

1 Introduction

Hydraulic fractures occur naturally during the spontaneous draining of glacial lakes, the calving of glaciers, the genesis of magma-driven dykes and sills, and the water-driven cracking of dams. Hydraulic fractures are also engineered by injecting a viscous fluid into rock to stimulate the rock for hydro-carbon extraction, for augmented geothermal energy production, for decontamination and disposal of waste water, and for preconditioning and cave inducement in mining operations. Once injection is stopped the wellbore is shut-in by closing a valve, or the fracture is allowed to bleed causing flow-back of fluid into the wellbore, or fluid is actively pumped from the wellbore. In this paper we consider the first of these injection cessation scenarios. At a smaller scale, miniature hydraulic fractures are also propagated and then allowed to recede for measurement and diagnostic purposes. During the evolution of these miniature fractures, the wellbore pressure is measured in order to estimate the leak-off coefficient or to identify the closure pressure to determine the minimum *in situ* stress σ_0.

After shut-in, depending on the various parameters characterizing the system including those controlling the fluid leak-off and the volume of injected fluid in the fracture at the time of shut-in, the hydraulic fracture may arrest almost immediately or may continue to propagate while the fluid pressure adjusts to the change in boundary condition at the wellbore. The unforced propagation will continue till the hydraulic fracture arrests when the stress intensity factor falls below the critical fracture toughness required for propagation. After arrest the fracture continues to deflate without altering its footprint while the stress intensity factor decreases to zero. Once the stress intensity factor is zero the fracture starts to recede until the point of collapse. This paper considers the deflation dynamics of a plane strain hydraulic fracture as it leaks fluid to the porous medium after shut-in.

Over the last five decades considerable research has been dedicated to building accurate models of propagating hydraulic fractures with the primary objective being to determine

the fracture footprint at shut-in. Since the formulation of some of the early models of hydraulic fractures propagating in a state of plane strain (see e.g. [23]), the seminal paper by Spence and Sharp [38] on self-similar solutions, and the landmark papers identifying the tip asymptotics of viscosity-dominated propagation [38, 25, 7], there has been considerable progress in the understanding of the tip asymptotics [17, 9, 2, 10] and the development of semi-analytic models of hydraulic fracture propagation [37, 13, 14]. The viscosity- and toughness-dominated analytic solutions have also been confirmed in precise laboratory experiments on translucent solids [4]. Multiscale tip asymptotic solutions have also been developed to capture multiple physical processes that may be active at the fracture tip [19, 15]. These asymptotic solutions enable the development of numerical algorithms [30, 31, 16] that have been shown to provide highly accurate solutions on extremely coarse meshes when compared to other techniques [24].

In contrast to the significant progress made in the modelling of propagating hydraulic fractures, there has, to our knowledge, been very little development of rigorous models of deflating hydraulic fractures both at arrest and during recession. Indeed, even the propagation of radially symmetric hydraulic fractures after shut-in has only recently been subjected to rigorous study [28]. This dearth of rigorous modelling exists despite the important role that modelling the arrest and recession deflation dynamics of hydraulic fractures plays in the interpretation of the borehole pressure decline to determine the leak-off coefficient and σ_0.

In the absence of a rigorous model for arrest and recession, current practice in leak-off identification [22, 29] assumes that the footprint of the hydraulic fracture during deflation remains the same as it was at the point of shut-in. In addition, without an accurate arrest and recession model it is difficult to locate the closure pressure from the pressure-time record to determine σ_0. Existing models of hydraulic fracture recession have been purely numerical and based on implementing a minimum aperture constraint [8, 1, 27, 21, 40]. Without a rigorous solution that accounts for the tip asymptotics of the

receding fracture, there is no way to assess the impact of the magnitude of the arbitrarily chosen minimum aperture on the numerical solution. There is thus a compelling need for a semi-analytic model that captures the deflation dynamics of a hydraulic fracture during arrest and recession. These models should make use of the appropriate tip solution obtained from rigorous analysis of the tip behaviour for a hydraulic fracture during arrest and recession.

This paper aims to address this issue for the case of a symmetric plane strain hydraulic fracture that deflates and recedes due to tip fluid losses to the porous medium. We make use of recent research [33] that has established the vertex asymptotic solutions for hydraulic fractures that deflate during the arrest and recession phases, as well as the multiscale asymptotic solutions that apply during arrest, through the transition between arrest and recession, and during recession itself.

In section 2, we describe the mathematical model and boundary and propagation conditions for a plane strain fracture that can propagate, deflate, and recede in a porous elastic medium. In section 3, we summarize the tip asymptotic behaviour for propagating hydraulic fractures, the multiscale arrest asymptotics, through the arrest-recession transition, and for recession. We also describe special fixed point iterative procedures that are required to implement the multiscale asymptotic solutions and demonstrate that the multiscale asymptotes are required to achieve smooth solutions through the arrest-recession transition point. In section 4, we present the scaling analysis and introduce the pair of novel dimensionless parameters, which make it possible to unify the power laws so that they apply for both zero and finite toughness cases. In section 5, we present numerical results that use the multiscale asymptotics to explore the impact of the dimensionless parameters on the time between shut-in and arrest, the duration of arrest, and the elapsed time from the initiation of arrest to collapse of the fracture. In section 6, we make some concluding remarks.

2 Mathematical Model

The mathematical model describing the dynamics of a fluid driven fracture needs to account for the dominant physical processes involved, namely: the deformation of the rock due to fracture opening; a mechanism for fracture growth; a description of the fluid-flow within the fracture; and the leak-off of fluid to the surrounding porous medium. In order that the model is tractable we make the following simplifying assumptions: the fracture propagates in a linear elastic solid characterized by the Young's modulus E and Poisson's ratio ν; growth of the fracture is assumed to be mode I according to linear elastic fracture mechanics (LEFM) and is modulated by fracture toughness K_{Ic}; fluid-flow within the fracture is assumed to be laminar, follows lubrication theory, and the fluid is assumed to be incompressible and Newtonian with a dynamic viscosity μ; a uniform far-field stress field σ_0 acts normal to the fracture; we restrict ourselves to leak-off governed by Carter's model [5] characterized by the leak-off coefficient C_L; we assume that the fluid and fracture fronts coalesce; and the solid medium is assumed to be homogeneous so that E, ν, K_{Ic}, and C_L are all constant.

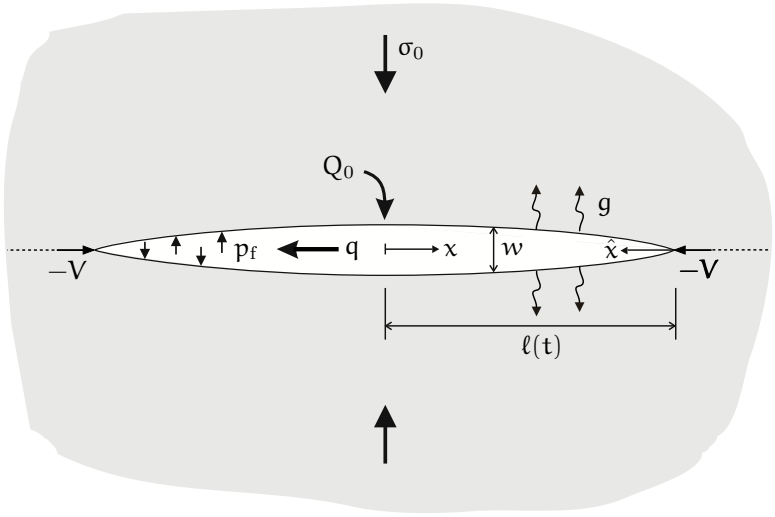

Figure 1: Schematic showing the KGD fracture geometry along with the coordinate systems used in the model

2.1 Governing Equations for a Plane Strain Hydraulic Fracture in a Permeable Medium

Since the solid medium is assumed to be homogeneous the fracture will grow symmetrically about the injection point. We choose to locate the origin of the x coordinate system at this point (see Figure 1). The primary unknowns in a hydraulic fracture problem are the fracture aperture $w(x,t)$, the fluid pressure $p_f(x,t)$ or the net pressure $p(x,t) = p_f(x,t) - \sigma_0$, the fluid flux $q(x,t)$, and the fracture half-length $\ell(t)$. The solution depends the injection rate $Q(t)$ (typically the volumetric injection rate divided by the height of the plane strain hydraulic fracture having dimensions $[Q] = L^2T^{-1}$) and four alternate material parameters, namely the plane strain modulus E', the alternate viscosity μ', the alternate fracture toughness K', and alternate Carter leak-off coefficient C', which are defined as follows in order to keep subsequent formulae uncluttered:

$$E' = \frac{E}{1-\nu^2},\ \mu' = 12\mu,\ K' = \left(\frac{32}{\pi}\right)^{1/2} K_{Ic},\ C' = 2C_L. \tag{1}$$

Elasticity: For a fracture with a half-length ℓ in an infinite, homogeneous, linear elastic solid in a state of plane strain, the fracture aperture w is the equilibrium elastic response to the imposed net pressure p, which are related by the following the integral equation:

$$p(x,t) = -\frac{E'}{4\pi}\int_{-\ell(t)}^{\ell(t)} \frac{\partial w}{\partial \xi}\frac{d\xi}{\xi - x} = -\frac{E'}{2\pi}\int_{0}^{\ell(t)} \frac{\partial w}{\partial \xi}\frac{\xi d\xi}{\xi^2 - x^2}. \tag{2}$$

Here the second integral in (2) can be obtained from the first by exploiting symmetry.

Continuity: Balance of fluid volume is expressed by the conservation law:

$$\frac{\partial w}{\partial t} + \frac{\partial q}{\partial x} + g = Q(t).\delta(x) \tag{3}$$

Here g represents the Carter leak-off velocity defined below. The point source is repre-

sented by the δ-function in (3) and we will be considering a propagation phase during which the fluid is injected at a constant rate Q_0 followed by a shut-in phase initiated at time t_s, after which time there is no further fluid injected into the fracture. Thus the source function $Q(t)$ can be expressed as

$$Q(t) = \begin{cases} Q_o & 0 < t < t_s \\ 0 & t \geqslant t_s. \end{cases}$$

Poiseuille's law: Assuming that the fracturing fluid is Newtonian and that the flow is laminar, the fluid flux inside the fracture can be expressed in terms of Poiseuille's law

$$q = -\frac{w^3}{\mu'}\frac{\partial p}{\partial x}. \tag{4}$$

Carter Leak-off law: We assume that the fluid loss to the permeable rock is captured by Carter's leak-off model [5]

$$g = \frac{C'}{\sqrt{t - t_o(x)}}. \tag{5}$$

in which $t_o(x)$ denotes the time of first exposure of point x to the fracturing fluid. This model excludes pressure-dependent leak-off, which is beyond the scope of this study. We observe that the Carter model (5) has a square root singularity at the tip if the fracture is propagating and exposing previously unfractured rock to the fracturing fluid. However, once the fracture has arrested or is receding, the leak-off term in (5) becomes finite. Indeed, the analysis presented in this paper is more general in that it only assumes that the leak-off function $g(x, t)$ is regular during arrest and recession.

Initial Conditions: The initial conditions are formally given by

$$\ell = 0, \quad w = 0, \quad p = 0, \quad \text{at } t = 0. \tag{6}$$

Boundary Conditions: For coalescent fluid and fracture fronts the boundary conditions

at the crack tips $x = \pm\ell$ are given by zero fracture opening and zero flux conditions [11]

$$w = 0, \quad q = 0, \qquad \text{at } x = \pm\ell. \tag{7}$$

For a symmetric fracture the δ-function source can be replaced by an equivalent flux boundary condition at $x = 0$

$$q(0^+, t) = \frac{Q(t)}{2}, \tag{8}$$

so that only half the fracture need be modelled.

Given these initial and boundary conditions, the fluid mass balance (3) and Carter leak-off law (5) can, after integrating both in time and space and exploiting symmetry, be expressed alternatively as the following global continuity equation:

$$2\int_0^{\ell(t)} w(x,t)\,dx + 4C'\int_0^{\ell(t)} \sqrt{t - t_o(x)}\,dx = V_f(t), \tag{9}$$

where

$$V_f = \begin{cases} Q_o t & 0 < t < t_s \\ V_o = Q_o t_s & t \geqslant t_s. \end{cases}$$

This equation simply establishes that the total volume of fluid injected at time t is equal to the volume of fluid contained in the crack plus the total volume of fluid lost to the permeable rock.

Propagation Condition: Since the fracture is assumed to propagate in limit equilibrium, linear elastic fracture mechanics (LEFM) [36] implies that the alternate mode-I stress intensity factor K satisfies the following inequality constraint:

$$K := E' \lim_{x \to \pm\ell} \frac{w}{\sqrt{\ell \mp x}} \leqslant K'. \tag{10}$$

Equality in (10) occurs when the fracture is propagating, i.e. $V > 0$, while strict inequal-

ity in (10) is associated with arrest characterized by $V = 0,\ 0 \leqslant K < K'$, and recession which is characterized by $V < 0$ and $K = 0$.

3 Tip Asymptotics for a HF in a Permeable Medium

3.1 Tip equations

Let $\hat{x} = \ell(t) - x$ denote a moving coordinate located on the tip of the crack with the $\hat{x}$-axis pointing inside the fracture (see Figure 1). Let $\hat{w}(\hat{x}, t)$, $\hat{p}(\hat{x}, t)$, and $\hat{q}(\hat{x}, t)$ denote the corresponding fracture aperture, net pressure, and flux referred to this new coordinate system. By convention, the flux $\hat{q}$ is taken positive when directed *opposite* to the $\hat{x}$-axis. Let $V(t)$ denote the fracture tip velocity, which is taken positive for a propagating fracture. Thus $\hat{q}$ and V have the same sign convention. In the moving coordinate system the governing equations become:

- Elasticity equation

$$\hat{p} = -\frac{E'}{4\pi} \int_0^{2\ell(t)} \frac{\partial \hat{w}}{\partial \hat{s}} \frac{d\hat{s}}{\hat{s} - \hat{x}}. \tag{11}$$

- Lubrication equation

$$\frac{\partial \hat{w}}{\partial t} + V \frac{\partial \hat{w}}{\partial \hat{x}} = \frac{\partial}{\partial \hat{x}} \left(\frac{\hat{w}^3}{\mu'} \frac{\partial \hat{p}}{\partial \hat{x}} \right) - \hat{g}, \quad 0 < \hat{x} < \ell(t). \tag{12}$$

We observe that the lubrication equation (12) is obtained by combining (3)-(5) with respect to variables in the $\hat{x}$ coordinate system. The boundary and propagation conditions are the shifted versions of those described above.

3.2 Local analysis and vertex solutions

Since we are interested in the behavior of the solution near the tip, we assume power law asymptotic solutions of the form:

$$\hat{w} \overset{\hat{x}\to 0}{\sim} A(t)\hat{x}^{\alpha},\ \frac{1}{2} \leqslant \alpha \leqslant 1, \tag{13}$$

The dominant behaviour [34] of the integral operator in (2) yields the following leading asymptotic behaviour for the net pressure

$$\hat{p} \sim \begin{cases} AE' \frac{\alpha}{4} \cot \pi\alpha \hat{x}^{\alpha-1},\ \frac{1}{2} < \alpha < 1 \\ \frac{AE'}{4\pi} \ln \hat{x},\ \alpha = 1 \end{cases} \tag{14}$$

and $\hat{p} = C$ for $\alpha = 1/2$. Now combining (13)-(14), the flux gradient can be expressed in the form

$$\frac{d\hat{q}}{d\hat{x}} \sim \begin{cases} \alpha(\alpha-1)(\alpha-\frac{1}{2}) \cot(\pi\alpha) \frac{A^4E'}{\mu'} \hat{x}^{4\alpha-3},\ \frac{1}{2} < \alpha < 1 \\ \frac{A^4E'}{2\pi\mu'} \hat{x},\ \alpha = 1 \end{cases} \tag{15}$$

Substituting the asymptotic relations (13)-(14) into (12) yields the following:

$$\dot{A}\hat{x}^{\alpha} + \alpha V A \hat{x}^{\alpha-1} - \alpha(\alpha-1)(\alpha-\frac{1}{2}) \cot(\pi\alpha) \frac{A^4E'}{\mu'} \hat{x}^{4\alpha-3} + \hat{g} = 0 :\ \frac{1}{2} < \alpha < 1, \tag{16}$$

$$\dot{A}\hat{x} + VA - \frac{A^4E'}{2\pi\mu'} \hat{x} + \hat{g} = 0 :\ \alpha = 1. \tag{17}$$

After arrest $V \leqslant 0$ and the leak-off term $\hat{g}$ is no longer singular since $t > t_0(x)$ for all points x within the fracture footprint, and so, as time progresses, it approaches a value that is spatially uniform. Thus, in order to perform the local analysis to determine asymptotic solutions after arrest, $\hat{g}$ will, to first order, be assumed to be spatially homogeneous in the tip region and denoted as $\hat{g}_0(t)$.

3.2.1 Propagation asymptotes ($K = K', V > 0$)

The vertex solutions for a propagating hydraulic fracture are well established [10]. The k'-asymptote associated with the fracture toughness is given directly by LEFM; the $\tilde{m}$-asymptote associated with leak-off is obtained by balancing the third and fourth terms in (16) with $\hat{g}$ approximated by $\hat{g} \sim C' \left(\frac{V}{\hat{x}}\right)^{1/2}$ close to the tip; the m-asymptote associated with viscous dissipation is obtained by balancing the second and third terms in (16). These asymptotes are respectively given by

$$\hat{w}_{k'} = l_{k'}^{1/2} \hat{x}^{1/2}, \ \hat{w}_{\tilde{m}} = \beta_{\tilde{m}} l_{\tilde{m}}^{3/8} \hat{x}^{5/8}, \ \hat{w}_{m} = \beta_{m} l_{m}^{1/3} \hat{x}^{2/3}, \tag{18}$$

where the following length scales have been defined: $l_{k'} = \left(\frac{K'}{E'}\right)^2$, $l_{\tilde{m}} = \left(\frac{4\mu' V C'^2}{E'}\right)^{1/3}$, and $l_m = \frac{\mu' V}{E'}$ and the constants are given by $\beta_{\tilde{m}} = 4/(15(\sqrt{2}-1))^{1/4}$ and $\beta_m = 2^{1/3}3^{5/6}$.

3.2.2 Arrest asymptotes ($0 \leqslant K < K', \ V = 0$)

The arrest asymptotes, recently described in [33], are: the k-asymptote $\hat{w}_k$ determined from LEFM in terms of the stress intensity factor K, which decreases from K' to 0 as fluid leaks from the fracture into the porous medium; and the ephemeral g-asymptote $\hat{w}_g$, associated with the arrest-recession transition, which is obtained by noting that $V = 0$ and matching the third and fourth terms in (16) with $\hat{g} \sim \hat{g}_0$. These asymptotes are respectively given by:

$$\hat{w}_k = l_k^{1/2} \hat{x}^{1/2} \text{ and } \hat{w}_g = \beta_g l_g^{1/4} \hat{x}^{3/4}, \tag{19}$$

where $l_k = \left(\frac{K}{E'}\right)^2 = \varepsilon_k^2 l_{k'}$ is the stress intensity length scale and ε_k is a dimensionless stress intensity parameter defined in terms of the stress intensity factor K as follows:

$$\varepsilon_k := \frac{K}{K'} = \frac{K_I}{K_{Ic}} < 1, \tag{20}$$

$l_g = \frac{\mu' \hat{g}_0}{E'}$ is the post-arrest leak-off length scale, and the constant $\beta_g = \left(\frac{64}{3}\right)^{1/4}$.

3.2.3 Recession asymptote - r-asymptote ($K = 0,\ V < 0$)

For $V < 0$, the g-asymptote with $\alpha = 3/4$ is inadmissible since the convective term $V\frac{\partial \hat{w}}{\partial \hat{x}}$, which is now nonzero, violates the dominant balance that applied when the fracture was at rest. Thus the only admissible balance occurs if $\alpha = 1$, for which the leading order match between the second and fourth terms in (17) yields the r-asymptote:

$$\hat{w}_r = \frac{\hat{g}_0}{|V|}\hat{x} = \frac{l_g}{l_r}\hat{x} = \frac{\hat{x}}{\varepsilon_r}, \tag{21}$$

where we have introduced the length scale $l_r = \frac{\mu'|V|}{E'}$ and the parameter $\varepsilon_r = \frac{|V|}{\hat{g}_0} = \frac{l_r}{l_g}$. There is also a match at the next order between the first and third terms in (17), respectively associated with the $\frac{\partial \hat{w}}{\partial t}$ and $\frac{\partial \hat{q}}{\partial \hat{x}}$ terms in the lubrication equation.

In [33] it has bee shown that by integrating (15) for the case $\alpha = 1$ and imposing the boundary condition $\hat{q}(0) = 0$ it follows that $\hat{q} > 0$, which, in the tip coordinate system $\hat{x}$, implies that fluid is moving towards the tip even though the crack is receding. This is consistent with the negative pressure gradients (with respect to the global coordinate x) that can be observed in figures 6 and 7, which imply that for receding fractures there is a flux of fluid toward the tip.

3.3 The connection problem to establish edge solutions

Vertex and multiscale tip asymptotic solutions [10, 19, 15] have proven to be extremely useful in the development of numerical algorithms to model propagating fractures [30, 2, 24, 31, 32, 16]. These algorithms can achieve solutions with a high degree of precision, able to account for the vertex and multiscale behaviour at the finest length scale, while using a relatively coarse mesh. The fundamental idea for propagating hydraulic fractures [30, 31, 16] is to use a trial value of the fracture aperture $\hat{w}$, sampled at computational

points within and adjacent to the fracture front, along with the applicable tip asymptote to estimate the fracture font location (or equivalently the local front velocity) at the current step. The front position for propagating fractures is then adjusted iteratively and the aperture updated until both are consistent with the applicable asymptote. The efficacy of this approach was clearly demonstrated in a collaborative study that evaluated a number of numerical algorithms [24] and benchmarked their relative accuracy against an analytic solution and compared their relative efficiency.

In the previous subsection we summarized the multiple vertex asymptotes that apply for hydraulic fractures propagating, at arrest, and receding - each corresponding to a different physical process that is assumed to be dominant at the tip. When multiple physical processes compete in the tip region then the asymptotic solution involves multiple vertex asymptotes. The multiscale solutions for propagating hydraulic fractures are well established [19, 15]. The multiscale tip solutions for the arrest and recession phases of a deflating hydraulic fracture were recently determined [33] by considering (11) and (12) in the limit $\hat{\mathrm{x}} \to 0$. These limiting equations [30] are those for a semi-infinite fracture in a state of plane strain that deflates while arrested $\mathsf{V} = 0$, or recedes with a constant velocity $\mathsf{V} < 0$. In this subsection we summarize these 'edge' solutions and discuss their implementation. In the numerical results provided in this section the Implicit Moving Mesh Algorithm (IMMA) described in [14] has been adapted to use the k and r-vertex asymptotes to model the arrest and recession phases and the results are compared to those obtained when the IMMA scheme is adapted to use the multiscale $\mathsf{k}-\mathsf{g}$ and $\mathsf{r}-\mathsf{g}$ edge solutions.

3.3.1 The $\mathrm{k}-\mathrm{g}$ edge solution:

Since $\hat{\mathrm{x}}^{1/2} \gg \hat{\mathrm{x}}^{3/4}$ as $\hat{\mathrm{x}} \to 0$, the k-asymptote will dominate the solution in the tip region and the g-asymptote will only manifest itself as we move farther from the tip. The extent of the region closest to the tip that is occupied by the k-asymptote decreases with K,

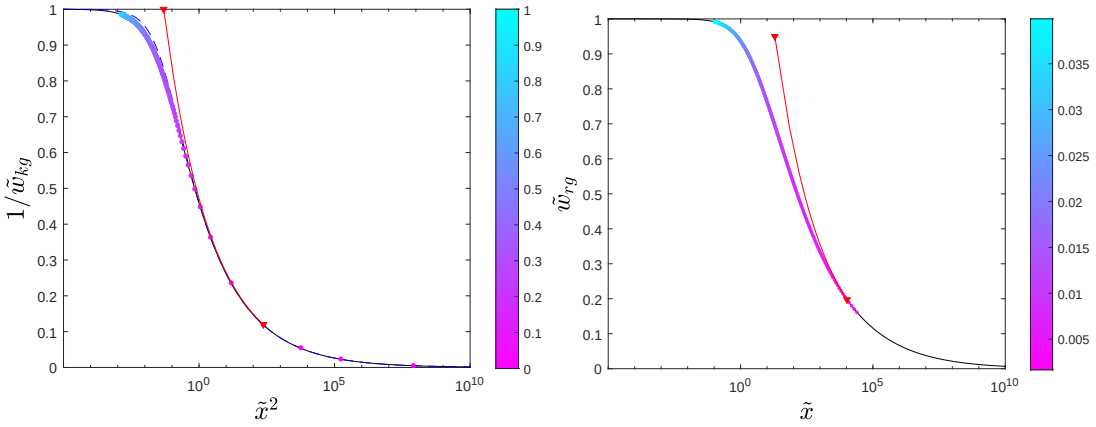

(a) $1/\tilde{w}_{\mathtt{kg}}$ vs $\tilde{\mathtt{x}}^2$ (b) $\tilde{w}_{\mathtt{rg}}$ vs $\tilde{\mathtt{x}}$

Figure 2: (a) Plot of the reciprocal of the scaled aperture $1/\tilde{w}_{\mathtt{kg}}$ as a function of $\tilde{\mathtt{x}}^2$ for the $\mathtt{k}-\mathtt{g}$ edge asymptote. The solid black curve represents the numerical solution to the coupled semi-infinite problem while the dashed blue curve represents the approximate solution provided by (22). (b) Plot of the scaled aperture $\tilde{w}_{\mathtt{rg}}$ as a function of $\tilde{\mathtt{x}}$ for the $\mathtt{r}-\mathtt{g}$ edge asymptote. The solid black curve represents the numerical solution to the coupled semi-infinite system. For both (a) and (b), the red curves between the inverted red triangles represent the search path for a single time step followed by the fixed point scheme (24) for $\varepsilon_{\mathtt{k}}$ (a) and the fixed point scheme (26) for $\varepsilon_{\mathtt{r}}$ (b). The coloured dots represent the solutions for $\varepsilon_{\mathtt{k}}$ and $\varepsilon_{\mathtt{r}}$ for multiple time steps.

while the fracture is deflating at arrest. The $\mathtt{g}$-asymptote expands into the tip region that has been vacated by the $\mathtt{k}$-asymptote until $\mathsf{K}=0$, at which instant the $\mathtt{g}$-asymptote occupies the tip region completely. We therefore seek the $\mathtt{k}-\mathtt{g}$ edge solution $\hat{w}_{\mathtt{kg}}$ that connects the inner solution $\hat{w} \overset{\hat{\mathtt{x}}\to 0}{\to} \hat{w}_{\mathtt{k}}$ to the outer solution $\hat{w} \overset{\hat{\mathtt{x}}\to\infty}{\to} \hat{w}_{\mathtt{g}}$.

Defining the length scale $\mathtt{l}_{\mathtt{kg}} = \frac{\mathtt{l}_{\mathtt{k}}^2}{\mathtt{l}_{\mathtt{g}}}$ and introducing the scaled variables $\tilde{\mathtt{x}} = \left(\frac{\hat{\mathtt{x}}}{\mathtt{l}_{\mathtt{kg}}}\right)^{1/2}$ and $\tilde{w}_{\mathtt{kg}} = \frac{\hat{w}_{\mathtt{kg}}}{\hat{w}_{\mathtt{k}}}$, the solution to the coupled problem for a deflating and arrested semi-infinite hydraulic fracture was given in [33]. The solution $\tilde{w}_{\mathtt{kg}}(\tilde{\mathtt{x}})$, which is universal in that it does not depend on any parameters, is denoted by the black curve in figure 2 (a). Assuming a power law behaviour for $\tilde{w}_{\mathtt{kg}}$ it is possible [33] to obtain the following explicit approximate solution, which has a relative error of less than 3% and is indicated

by the dashed blue curve in figure 2 (a).

$$\tilde{w}_{k g} \approx \left(1+\beta_{g}^{4} \tilde{x}^{2}\right)^{1 / 4} \text { or } \hat{w}_{k g} \approx l_{k}^{1 / 2} \hat{x}^{1 / 2}\left(1+\beta_{g}^{4} \frac{\hat{x}}{l_{k g}}\right)^{1 / 4} . \tag{22}$$

Assuming that $\tilde{w}_{k g}(\tilde{x})$ is a known function of $\tilde{x}$, the scalings defined above can be used to obtain the following relationship between $\hat{w}$ and $\hat{x}$ for the $k-g$-asymptote:

$$\hat{w}=\hat{w}_{k}(\hat{x}) \tilde{w}_{k g}\left((\frac{\hat{x}}{l_{k g}})^{1 / 2}\right)=\varepsilon_{k} \hat{w}_{k^{\prime}}(\hat{x}) \tilde{w}_{k g}\left(\frac{1}{\varepsilon_{k}^{2}}(\frac{\hat{x}}{l_{k^{\prime} g}})^{1 / 2}\right), \tag{23}$$

where $l_{k}=\varepsilon_{k}^{2} l_{k^{\prime}}$, $l_{k g}=\varepsilon_{k}^{4} l_{k^{\prime} g}$, and $l_{k^{\prime} g}=\frac{l_{k^{\prime}}^{2}}{l_{g}}$. Thus given trial values of $\hat{w}$, sampled a certain distance $\hat{x}$ from the tip, (23) defines ε_{k}, and therefore K, implicitly.

A robust fixed point iterative scheme for ε_{k} [35] can be obtained by re-writing (23) in the following recursive form:

$$\varepsilon_{k, i+1}=\frac{\hat{w}}{l_{k^{\prime}}^{1 / 2} \hat{x}^{1 / 2}} \frac{1}{\tilde{w}_{k g}\left(\frac{1}{\varepsilon_{k, i}^{2}}(\frac{\hat{x}}{l_{k^{\prime} g}})^{1 / 2}\right)} . \tag{24}$$

Note that this recursion is expressed in terms of the function $0 \leqslant 1 / \tilde{w}_{k g} \leqslant 1$ plotted in figure 2 (a). The red curve in this figure represents the trajectory of iterates $\varepsilon_{k, i}$ for a particular time step, which is selected to be later in the deflation process as it is associated with a small value of ε_{k}. This sequence of iterates starts with the initial guess $\varepsilon_{k, 0}=\frac{\hat{w}}{l_{k^{\prime}}^{1 / 2} \hat{x}^{1 / 2}}$, which is obtained from the LEFM asymptote given in the first expression in (19), and indicated in figure 2 (a) by the inverted red triangle for which $1 / \tilde{w}_{k g} \sim 1$. These iterations terminate when the relative difference between successive iterates is less than 10^{-3} at the point indicated by the inverted red triangle on the lower part of the red curve. The coloured circles moving down the $1 / \tilde{w}_{k g}$ curve in (a) represent the sequence of decreasing ε_{k} values (with values depicted on the colour bar), which correspond to decaying K values over multiple time steps as the fracture deflates while arrested.

3.3.2 The $r-g$ edge solution:

Because $\hat{x}^{3/4} \gg \hat{x}$ as $\hat{x} \to 0$, we would expect the g-asymptote to dominate the r-asymptote closest to the tip. However, since the g-asymptote cannot exist at the tip for $V < 0$, it is the r-asymptote that occupies the region closest to the tip while the g-asymptote will only manifest itself farther from the tip. Thus, as recession begins, i.e. $V < 0$, the g-asymptote, which occupied the tip region completely at the instant $K = 0$, is immediately displaced from the tip by the r-asymptote. We therefore seek the $r-g$ edge solution $\hat{w}_{rg}$ that connects the inner solution $\hat{w} \overset{\hat{x}\to 0}{\to} \hat{w}_r$ to the outer solution $\hat{w} \overset{\hat{x}\to\infty}{\to} \hat{w}_g$.

Defining the length scale $l_{rg} = \frac{l_r^4}{l_g^3}$ and introducing the scaled variables $\tilde{x} = \frac{\hat{x}}{l_{rg}}$ and $\tilde{w}_{rg} = \frac{\hat{w}_{rg}}{\hat{w}_r}$, the solution to the coupled problem for a semi-infinite hydraulic fracture receding with a constant velocity $V < 0$ is given in [33]. The solution $\tilde{w}_{rg}(\hat{x})$, which is also universal in that it does not depend on any parameters, is denoted by the black curve in figure 2 (b). Assuming that $\tilde{w}_{rg}$ is a known function of $\tilde{x}$, we can use the above scalings to obtain the following relationship between $\hat{w}$ and $\hat{x}$ for the $r-g$-asymptote:

$$\hat{w} = \hat{w}_r(\hat{x}) \left(\tilde{w}_{rg} \left(\frac{\hat{x}}{l_{rg}} \right) \right) = \frac{\hat{x}}{\varepsilon_r} \left(\tilde{w}_{rg} \left(\frac{\hat{x}}{\varepsilon_r^4 l_g} \right) \right), \tag{25}$$

where $l_r = \varepsilon_r l_g$ and $l_{rg} = \varepsilon_r^4 l_g$. Thus given trial values of $\hat{w}$, sampled a certain distance $\hat{x}$ from the tip, (25) defines ε_r, and therefore $|V|$, implicitly. A robust fixed point iterative scheme for ε_r can be obtained by re-writing (25) in the following recursive form [35]:

$$\varepsilon_{r,i+1} = \frac{\hat{x}}{\hat{w}} \left(\tilde{w}_{rg} \left(\frac{\hat{x}}{\varepsilon_{r,i}^4 l_g} \right) \right). \tag{26}$$

Note that this recursion is expressed in terms of the function $0 \leqslant \tilde{w}_{rg} \leqslant 1$ plotted in figure 2 (b). The red curve in this figure represents the trajectory of iterates $\varepsilon_{r,i}$ for a time step, which is selected to be early in the recession because it is associated with a small value of ε_r. This sequence of iterates starts with the initial guess $\varepsilon_{r,0} = \frac{\hat{x}}{\hat{w}}$,

which is obtained from r-asymptote (21), and indicated by the inverted red triangle at which $\tilde{w}_{rg} \sim 0.95$. These iterations terminate when the relative difference between successive iterates is less than 10^{-3} at the point indicated by the inverted red triangle on the lower part of the red curve. The coloured circles moving up the $\tilde{w}_{rg}$ curve in (b) represent the sequence of increasing ε_r values (with values depicted on the colour bar), which correspond to increasing $|V|$ values over multiple time steps as the receding fracture accelerates from the point of arrest.

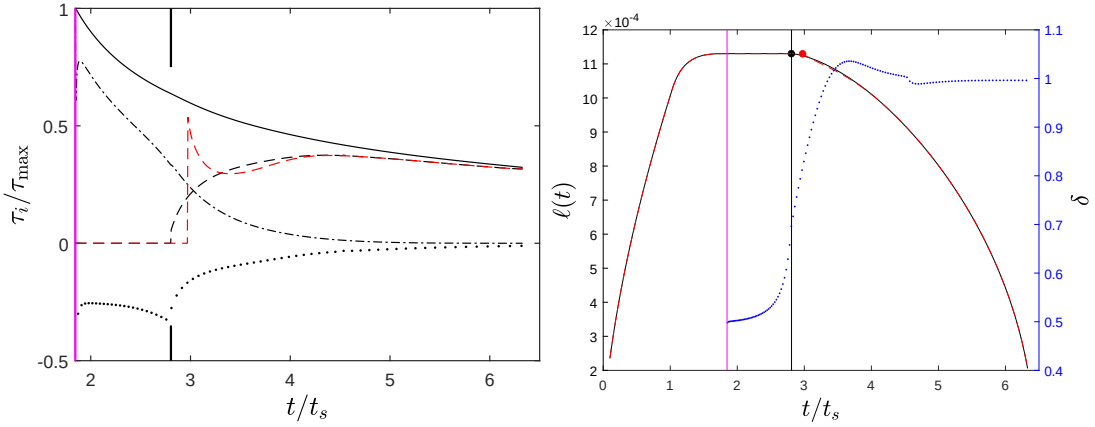

(a) Balance of terms

(b) $\ell(t)$ and δ vs t

Figure 3: (a) Evolution of terms in the continuity equation from arrest to collapse $t \in (t_a, t_c)$ scaled to the maximum value on this interval: flux gradient $\frac{\partial \hat{q}}{\partial \hat{x}}$ $(-\cdot)$, $\frac{\partial \hat{w}}{\partial t}$ $(\cdots)$, $|V|\frac{\partial \hat{w}}{\partial \hat{x}}$ $(--)$, and $\hat{g}_0$ (solid). The black curves are extracted from an IMMA simulation that uses the multiscale $k-g$ and $r-g$-asymptotes, while the dashed red curve represents the convection term $|V|\frac{\partial \hat{w}}{\partial \hat{x}}$ when the simple LEFM k-asymptote is used to determine the stress intensity factor during arrest and only the linear r-asymptote is used to determine the negative velocity during recession. (b) The fracture length $\ell(t)$ is plotted against t for two different IMMA simulations, one using the mulitscale $k-g$ and $r-g$-asymptotes (solid black) and the other (dashed red) using the simple LEFM k-asymptote to determine the stress intensity factor during arrest and the linear r-asymptote to determine the negative velocity during recession. The blue dots represent estimates of the power law behaviour of $\hat{w}$ in the tip region from the formula $\delta = \frac{\hat{x}\frac{\partial \hat{w}}{\partial \hat{x}}}{\hat{w}}$.

3.3.3 The arrest/recession transition and the emergence of a dominant balance

Magnitude of terms in the lubrication equation:

In figure 3 (a) we compare the relative magnitudes of each of the terms in the continuity equation (12) as a function of t/t_s from the time of arrest t_a to the time of collapse t_c. To establish the relative magnitudes, each of the terms τ_i in the continuity equation is divided by the maximum value $\tau_{max} = \max_{t\in(t_a,t_c)} \max_{i} |\tau_i(t)|$ over the interval. The arrest time t_a is indicated in this plot by the vertical magenta line, while the arrest/recession transition point t_r is indicated by the thick black vertical lines that have been separated in order that the results of the plot are not obscured.

Comparison between IMMA solutions using edge asymptotes vs vertex asymptotes:

The black curves in figure 3 (a) represent the IMMA results obtained when the multiscale $k-g$ edge solution has been used to determine ε_k (and hence the stress intensity factor for the arrested deflating fracture) and the arrest/recession transition point t_r, and the $r-g$ edge solution has been used to determine ε_r and the magnitude of the receding fracture velocity. We will refer to this combined solution as *the multiscale edge* solution. The dashed red curve represents the IMMA result for the convective term $|V|\frac{\partial \hat{w}}{\partial \hat{x}}$ obtained when the simple LEFM k-asymptote given in the first equation in (19) is used to determine ε_k and the arrest/recession transition point t_r, while the linear r-asymptote is used to determine ε_r. We will refer to this combined solution as *the vertex* solution. We have chosen to restrict the comparison between these two different IMMA solutions to the convective term since this term exhibits the largest difference between the two solutions and to keep the plot uncluttered. The solution (black ——) that uses multiscale edge asymptotes through the transition point t_r is much smoother than the corresponding vertex solution (red ——). Indeed, the vertex solution has a delayed transition point that exhibits an extreme jump discontinuity and a subsequent sharp drop to compensate until the transient effect of neglecting this multiscale behaviour decays around $t/t_s \sim 4$.

The reason that using the $\mathfrak{r}$-vertex solution (21) over-estimates $\varepsilon_{\mathfrak{r}}$, and therefore the recession speed, is that it immediately attributes *all* the fracture aperture in the tip region to the linear asymptote. However, we know that, at the transition point $\mathfrak{t}_{\mathfrak{r}}$, the tip is fully occupied by the stationary $\mathfrak{g}$-asymptote. Therefore, it takes some time for the linear $\mathfrak{r}$-asymptote, which is initially only valid on a very small length scale, to displace this $\mathfrak{g}$-asymptote and occupy the tip at the length scale of one computational cell. Thus using the $\mathfrak{r}$-asymptote immediately upon the initiation of recession, without waiting for the linear asymptote to occupy the tip element, is the cause of the observed jump in the convective term. By contrast, the multiscale edge solution is able to accumulate the appropriate amount of the $\mathfrak{g}$-vertex in the tip apertures while the arrested fracture is deflating and, upon the initiation of recession, it is able to distribute the tip aperture correctly between the stationary $\mathfrak{g}$-vertex and the moving $\mathfrak{r}$-vertex and thereby identify the correct recession velocity.

Exponent evolution:

As a measure of the exponent of the average power law active in the tip region for the multiscale edge solution, we calculate the quotient $\delta = \frac{\hat{x}\frac{\partial \hat{w}}{\partial \hat{x}}}{\hat{w}}$ in the tip element, which, for a power law, would yield the value of the exponent. The derivative in this quotient is approximated by the second order backward difference approximation involving the three elements closest to the tip. The evolution of δ over the interval $t \in (t_a, t_c)$ is represented by the blue dots referenced to the right vertical axis in figure 3 (b). As in (a) the arrest time horizon t_a is indicated in this plot by the vertical magenta line, while the arrest/recession transition horizon t_r is indicated by the vertical black line. We observe that δ evolves from the LEFM exponent of 1/2 at the beginning of the arrest period, then passes through the g-vertex exponent 3/4 close to the arrest/recession transition point t_r, and finally asymptotes to the r-vertex exponent 1 for $t/t_s \gtrsim 4$.

The emergence of a dominant balance:

We observe from figure 3 (a) that between the arrest time t_a, indicated by the vertical magenta line, and $t \sim 4t_s$ there is no dominant balance in that no two (or three) terms form a dominant pair (triplet) so that their magnitudes match and they dominate the other terms in the lubrication equation. Such a dominant balance would lead to a vertex asymptotic solution. However, for $t_a \leqslant t \lesssim 4t_s$ there is a mixture of interacting terms indicating that the tip is governed by multiscale tip asymptotics and not a single vertex solution. However, beyond $t/t_s \sim 4$, a leading order match emerges between the second term $|V|\frac{\partial \hat{w}}{\partial \hat{x}}$ and the fourth term $\hat{g}$ in the lubrication equation (12). These were precisely the terms used in the dominant balance argument to establish the r-vertex solution (21). We also note that the two terms $\frac{\partial \hat{w}}{\partial t}$ and $\frac{\partial \hat{q}}{\partial \hat{x}}$ that were found to match at the next order can also be seen to asymptote to much smaller values than those of the dominant match, but of a comparable magnitude to one another.

Impact of using vertex asymptotes rather than edge asymptotes:

From figure 3 (a) and the discussion above we see that using the vertex asymptotes to track the deflation of the hydraulic fracture results in the jump discontinuity in the velocity as one passes through the arrest/recession transition $\mathtt{t_r}$. Although the existence of the $\mathtt{g}$-vertex is ephemeral, we see that it is necessary to account for this special solution in both the multiscale $\mathtt{k}-\mathtt{g}$ and $\mathtt{r}-\mathtt{g}$ edge solutions in order to obtain a solution that will pass smoothly through the arrest/recession transition $\mathtt{t_r}$. However, from figure 3 (a) we also observe that, if we use only the vertex asymptotes, the transients that result from the jump discontinuity decay fairly rapidly and the solution reverts to the same smooth solution produced by the multiscale edge asymptotes. These transients decay on roughly the same time scale as the emergence of a dominant balance between the convection and leak-off terms. Since this latter balance was associated with the $\mathtt{r}$-vertex solution it is not surprising that the numerical solution that uses only vertex asymptotes starts to converge to the multiscale solution at this stage of the recession phase.

Rather than only using individual terms in the lubrication equation to assess the impact of implementing simple vertex asymptotes as opposed to multiscale edge asymptotes on the quality of the solution, we also consider a more global quantity such as the fracture length. In figure 3 (b) we compare the fracture length $\ell(\mathtt{t})$ as a function of $\mathtt{t}/\mathtt{t_s}$ for the multiscale algorithm (solid black) to that for the simple vertex algorithm (dashed red). The transition point $(\mathtt{t_r}/\mathtt{t_s}, \ell(\mathtt{t_r}))$ from arrest to recession for the multiscale solution is denoted by the black circle and that for the simple vertex asymptotes is denoted by the red circle. The vertex solution only has a slightly delayed recession initiation time and exhibits only a slight deviation from the multiscale edge solution, which starts immediately after the onset of recession and persists until the transients decay. Indeed, these two solutions differ by less than $\frac{1}{2}$ % throughout the duration of the simulation and are virtually indistinguishable in figure 3 (b).

The analysis presented here has been important in order to provide a rigorous mul-

tiscale solution for the deflation of a hydraulic fracture during arrest and recession and particularly around the arrest/recession transition time t_r. However, this analysis also establishes that, unless the purpose of the modelling is to provide a smooth solution with great detail around the arrest/recession transition point t_r, a pragmatic and much more efficient approach would be to use a simpler algorithm based solely on vertex asymptotes.

4 Scaling Analysis

4.1 Scaling

4.1.1 Scaling for a KGD fracture subject to a constant injection rate Q_0

Following [9, 10] we introduce the length scale ℓ_* and time scale t_* and characteristic aperture w_* and net pressure p_* such that $x = \ell_* \xi$, $t = t_* \tau$, $w = w_* \Omega$, and $p = p_* \Pi$ into the governing equations (2)-(5), enabling us to identify the following five dimensionless groups:

$$\mathcal{G}_v = \frac{\ell_* w_*}{Q_0 t_*},\ \mathcal{G}_m = \frac{\ell_* \mu' Q_0}{w_*^3 p_*},\ \mathcal{G}_c = \frac{C' \ell_*}{t_*^{1/2} Q_0},\ \mathcal{G}_e = \frac{E' w_*}{\ell_* p_*},\ \text{and } \mathcal{G}_k = \frac{K' \ell_*^{1/2}}{E' w_*}. \tag{27}$$

The viscous m-scaling can be identified by requiring $\mathcal{G}_v = \mathcal{G}_m = \mathcal{G}_e = 1$, from which it follows that the length ℓ_m, aperture w_m, and pressure p_m scales are respectively given by

$$\ell_m = \left(\frac{E' Q_0^3 t^4}{\mu'}\right)^{1/6},\ w_m = \left(\frac{\mu' Q_0^3 t^2}{E'}\right)^{1/6}, \text{and } p_m = \left(\frac{\mu' E'^2}{t}\right)^{1/3}, \tag{28}$$

while the dimensionless toughness and leak-off coefficient become

$$\mathcal{G}_k := \mathcal{K}_m = \left(\frac{K'^4}{E'^3 \mu' Q_0}\right)^{1/4},\ \text{and } \mathcal{G}_c := \mathcal{C}_m(t) = \left(\frac{C'^6 E' t}{\mu' Q_0^3}\right)^{1/6}. \tag{29}$$

The leak-off ($\tilde{m}$-scaling) can be obtained by requiring $\mathcal{G}_c = 1$ instead of $\mathcal{G}_v$ and the toughness (k-scaling) can be obtained by requiring $\mathcal{G}_k = 1$ instead of $\mathcal{G}_m$. We observe

from (29) that the dimensionless toughness for a KGD fracture driven by a constant injection rate Q_0 is independent of time, while the dimensionless leak-off coefficient increases with time. From (29) we observe that the transition time $t_{m\tilde{m}}$ from storage dominated propagation to leak-off dominated propagation is given by

$$t_{m\tilde{m}} = \frac{\mu' Q_0^3}{C'^6 E'}. \tag{30}$$

4.1.2 Scaling for a KGD fracture after shut-in

The injection of fluid at a constant flux Q_0 is followed by shut-in at a certain time t_s. Propagation of the hydraulic fracture, initiated at the beginning of the injection phase, may continue after shut-in depending on the regime of propagation. A propagating fracture in a permeable medium will ultimately come to rest either due to excessive leak-off if $K' = 0$ or because the stress intensity factor K has dropped below the fracture toughness K'. There is an arrest period during which K decreases as the fracture continues to lose fluid to the porous medium so that $\dot{w} < 0$, until transition to the recession asymptote is initiated when $K = 0$ and the fracture starts to recede. However, if the hydraulic fracture is already in the leak-off regime at the time of shut-in, then recession can be expected to start almost immediately after arrest.

The appropriate scaling for the dynamics with a fixed injected volume V_0 per unit height of the plain strain hydraulic fracture can be obtained [28] directly from those of a fracture driven by a constant flux Q_0 given in (28)-(29) by making the simple substitution $Q_0 = V_0/t$. In this case the length $\ell_m^V(t)$ and aperture $w_m^V(t)$ scaling factors are given by

$$\ell_m^V(t) = \left(\frac{E' V_0^3 t}{\mu'}\right)^{1/6} \text{ and } w_m^V(t) = \left(\frac{\mu' V_0^3}{E' t}\right)^{1/6}, \tag{31}$$

while the dimensionless toughness $\mathcal{K}_m^V(t)$ and leak-off $\mathcal{C}_m^V(t)$ parameters become

$$\mathcal{K}_m^V(t) = \left(\frac{K'^4 t}{E'^3 \mu' V_0}\right)^{1/4} \text{ and } \mathcal{C}_m^V(t) = \left(\frac{C'^6 E' t^4}{\mu' V_0^3}\right)^{1/6}. \tag{32}$$

Here we have followed Mori and Lecampion [28] and used the superscript V to denote the scaling for a fracture with a fixed shut-in volume V_0 at time t. Note that for the propagation of a KGD fracture with a fixed shut-in volume, in contrast to the case of a constant injection rate, the dimensionless toughness $\mathcal{K}_m^V(t)$ is time dependent. We observe from (32) that for a KGD fracture with a fixed shut-in volume V_0, the viscous to toughness transition time t_{mk}^V and viscosity-storage to leak-off transition time $t_{m\tilde{m}}^V$ are respectively given by

$$t_{mk}^V = \frac{E'^3 \mu' V_0}{K'^4} \text{ and } t_{m\tilde{m}}^V = \left(\frac{\mu' V_0^3}{C'^6 E'}\right)^{1/4}. \tag{33}$$

Once shut-in has occurred these two transition times identify two different ways the fracture behaves after the time of arrest t_a, which, if $K' > 0$, is characterized by the stress intensity factor dropping below the critical fracture toughness and, as a result, the velocity of the fracture going to zero. If $t_a \sim t_{mk}^V \ll t_{m\tilde{m}}^V$, then at the time of arrest the fracture is propagating in the toughness regime and still has a significant amount of fluid that needs to leak-off before recession can start. Conversely, if $t_a \sim t_{m\tilde{m}}^V \ll t_{mk}^V$, then at the time of arrest the fracture is propagating in the leak-off regime and has lost sufficient fluid to preclude significant further propagation of the fracture. In this case recession starts almost immediately. In order to characterize these two arrest modes, we define the following arrest regime parameter ϕ^V for a fixed injected volume KGD hydraulic fracture

$$\phi^V = \frac{t_{mk}^V}{t_{m\tilde{m}}^V} = \left(\frac{E'^{13} \mu'^3 C'^6 V_0}{K'^{16}}\right)^{\frac{1}{4}}. \tag{34}$$

If $\phi^V \gg 1$ then the transition to leak-off dominated propagation will occur significantly

before there would be transition to toughness dominated propagation, so recession can be expected to start almost immediately and there will be a short arrest period. Conversely, if $\phi^V \ll 1$ then the transition to toughness dominated propagation will occur while the fracture is in the storage regime significantly before there would be a transition to leak-off dominated propagation. Thus at the time of arrest there is still a significant volume of fluid contained in the fracture that needs to leak off before recession can begin. Thus in this case there will be a significant period during which the fracture deflates while it is in a state of arrest. We observe that the parameter ϕ^V defined in (34) has no meaning in the zero toughness case since $t^V_{mk} = \infty$.

4.2 Characteristic Power Laws for arrest and recession

In the analysis that follows we consider a given shut-in time t_s, which we define with respect to the constant injection rate storage-leak-off transition time $t_{m\tilde{m}}$ in terms of the parameter ω defined by

$$\omega = \frac{t_s}{t_{m\tilde{m}}}. \tag{35}$$

At shut-in, the injected volume is $V_s = Q_0 t_s$, the dimensionless leak-off coefficient $\mathcal{C}_m(t_s) := \mathcal{C}_s = \omega^{1/6}$, while the constant injection rate dimensionless toughness $\mathcal{K}_m := \mathcal{K}_s$ remains constant throughout injection. The fixed injected volume transition times, at which $\mathcal{K}^V_m(t) = 1$ and $\mathcal{C}^V_m(t) = 1$, can be expressed in terms of $\mathcal{K}_s$ and $\mathcal{C}_s$ as follows:

$$t^V_{mk} := t_s \mathcal{K}_s^{-4} \text{ and } t^V_{m\tilde{m}} := t_s \mathcal{C}_s^{-3/2}. \tag{36}$$

Now making use of (30) and (33) the following relationship can be established between the fixed injected volume transition time $t^V_{m\tilde{m}}$ and the constant injection rate storage-leak-off transition time $t_{m\tilde{m}}$ in terms of the dimensionless shut-in parameter ω :

$$t^V_{m\tilde{m}} = t_{m\tilde{m}} \omega^{\frac{3}{4}} = t_s \omega^{-\frac{1}{4}}, \tag{37}$$

where the second relationship in (37) comes directly from the definition of ω.

Modes of arrest and recession: Using (37) and (34) we are now able to characterize the way in which the arrest time t_a and recession time t_r are impacted by the relative magnitudes of ϕ^V and ω.

- If $\phi^V \ll 1$:
  - If $\omega \ll 1$, it follows from (37) and (34) that

$$t_s \;\&\; t^V_{mk} \ll t^V_{m\tilde{m}} \ll t_{m\tilde{m}},$$

    then, after shut-in, arrest will be determined by $t_a \sim t^V_{mk}$ and recession will be determined by $t_r \sim t^V_{m\tilde{m}}$.
  - If $\omega \gg 1$, it follows from (37) and (34) that

$$t_{m\tilde{m}} \;\&\; t^V_{mk} \ll t^V_{m\tilde{m}} \ll t_s,$$

    then, after shut-in, arrest and recession will be determined by $t_a \sim t_r \sim t_s$.
- If $\phi^V \gg 1$:
  - If $\omega \ll 1$, it follows from (37) and (34) that

$$t_s \;\ll t^V_{m\tilde{m}} \ll t_{m\tilde{m}} \;\&\; t^V_{mk},$$

    then, after shut-in, arrest and recession will be determined by $t^V_{m\tilde{m}}$, i.e. $t_a \sim t_r \sim t^V_{m\tilde{m}}$.
  - If $\omega \gg 1$, it follows from (37) and (34) that

$$t_{m\tilde{m}} \;\ll t^V_{m\tilde{m}} \ll t_s \;\&\; t^V_{mk},$$

then, after shut-in, arrest and recession will be determined by $t_a \sim t_r \sim t_s$.

4.2.1 Zero Toughness Case ($K' = 0$)

From (34) it follows that if $K' \to 0$ then $\phi^V \to \infty$, which, from the modes of arrest and recession identified above, clearly identifies the scaling for the time of arrest t_a, which, in this case, coincides with that of recession.

Arrest Scaling: If the dimensionless shut-in time $\omega \ll 1$ then the arrest time t_a is determined by the time that the fixed volume fracture transitions from storage to leak-off dominated propagation, i.e.

$$t_a \sim t^V_{m\tilde{m}} = t_s \mathcal{C}_s^{-3/2} = t_s \omega^{-1/4}. \tag{38}$$

The corresponding length and aperture scales, $\ell_a := \ell^V_m(t_a)$ and $w_a := w^V_m(t_a)$, can be expressed in terms of ω, $\ell_s := \ell_m(t_s)$, and $w_s := w_m(t_s)$ as follows:

$$\ell_a = \left(\frac{E' V_0^5}{\mu' C'^2}\right)^{1/8} = \ell_s \omega^{-1/24} \text{ and } w_a = \left(\frac{\mu' C'^2 V_0^3}{E'}\right)^{1/8} = w_s \omega^{1/24}. \tag{39}$$

If $\omega \gg 1$, then shut-in occurs considerably later than the constant injection rate storage-leak-off transition time $t_{m\tilde{m}}$, so arrest can be expected to occur shortly after shut-in. These two limiting scalings can be summarized as follows:

$$t_a/t_s \sim \begin{cases} \omega^{-1/4} \text{ if } \omega \ll 1 \\ 1 \quad \text{if } \omega \gg 1 \end{cases}, \tag{40}$$

$$\ell_a/\ell_s \sim \begin{cases} \omega^{-1/24} \text{ if } \omega \ll 1 \\ 1 \text{ if } \omega \gg 1 \end{cases}, \tag{41}$$

$$w_a/w_s \sim \begin{cases} \omega^{1/24} \text{ if } \omega \ll 1 \\ 1 \text{ if } \omega \gg 1 \end{cases}. \tag{42}$$

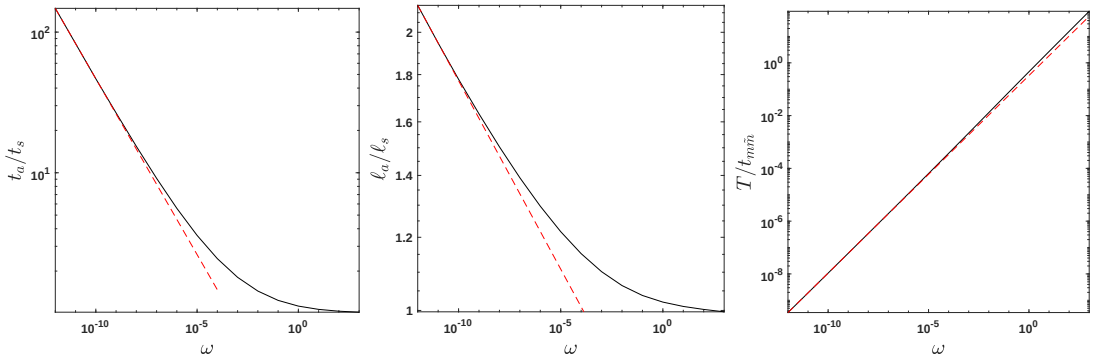

(a) t_a/t_s vs ω (b) ℓ_a/ℓ_s vs ω (c) $T/t_{m\tilde{m}}$ vs ω

Figure 4: The solid black lines indicate the numerical solutions for the: (a) arrest time to shut-in time ratios, (b) arrest length to shut-in length ratios, and (c) deflation time to storage-leak-off transition time ratios $T/t_{m\tilde{m}}$ all plotted as a function of ω for the zero toughness case $K' = 0$. The dashed red lines represents log linear regressions for each of these plots using the first few data points.

Results of numerous simulations using the IMMA algorithm are reported in figure 4 for the zero toughness case. The plots show the variation of t_a/t_s, ℓ_a/ℓ_s, and $T/t_{m\tilde{m}}$ (where $T = t_c - t_a$ is the deflation time) as functions of the dimensionless shut-in time ω. The red line in each plot represents the power law $A\omega^{\alpha}$ with coefficient A and index α computed by a log linear regression for a few data points corresponding to the smallest values of ω. The regression yields $\alpha = -0.25$ for the ratio t_a/t_s, which is consistent with the power law (40), and $\alpha = -0.041$ for the ratio ℓ_a/ℓ_s, which is again consistent with the power law (41).

Deflation Time Scaling: Motivated by the recession asymptote, in which the dominant balance is between the term representing the rate of change of aperture and the leak-off term, we consider the following model to estimate the deflation time T

$$\frac{\partial w}{\partial t'} \sim \frac{C'}{\sqrt{T - t'}}, \tag{43}$$

where we define the reverse time variable to be $t' = t_c - t$. Integrating (43), it follows that $w \sim C'\sqrt{T}$ at time $t' = T$ ($t = t_a$). Then equating this aperture to $w_m^V(t_a)$, and

using the fact that $w_s = C' t_{m\tilde{m}}^{1/2} \omega^{1/3}$, it follows that

$$T \sim t_{m\tilde{m}} \omega^{3/4} \tag{44}$$

The dashed red line in figure 4 (c) represents a log linear regression of $T/t_{m\tilde{m}} \sim A\omega^{\alpha}$ in which $\alpha = 0.749$, which is very close to the power law (44) predicted by the scaling analysis.

4.2.2 Finite Toughness Case ($K' > 0$)

Arrest Scalings: If the dimensionless shut-in time $\omega \ll 1$, then the arrest time t_a is determined by when the fracture transitions from viscosity to toughness dominated propagation, which according to (34) occurs when

$$t_a \sim t_{mk}^{V} = \phi^{V} t_{m\tilde{m}}^{V} = t_s \phi^{V} \omega^{-1/4}. \tag{45}$$

As with the zero toughness case, the corresponding length and aperture scales can be obtained by substituting t_a into (31). If $\omega \gg 1$ then shut-in occurs considerably later than the constant injection rate storage-leak-off transition time $t_{m\tilde{m}}$, so arrest can be expected to occur shortly after shut-in. These two limiting scalings can be summarized as follows:

$$t_a/t_s \sim \begin{cases} \phi^{V} \omega^{-1/4} \text{ if } \omega \ll 1 \\ 1 \quad \text{if } \omega \gg 1 \end{cases}, \tag{46}$$

$$\ell_a/\ell_s \sim \begin{cases} \left(\phi^{V}\right)^{1/6} \omega^{-1/24} \text{ if } \omega \ll 1 \\ 1 \text{ if } \omega \gg 1 \end{cases}, \tag{47}$$

$$w(t_a)/w_s \sim \begin{cases} \left(\phi^{V}\right)^{-1/6} \omega^{1/24} \text{ if } \omega \ll 1 \\ 1 \text{ if } \omega \gg 1 \end{cases}. \tag{48}$$

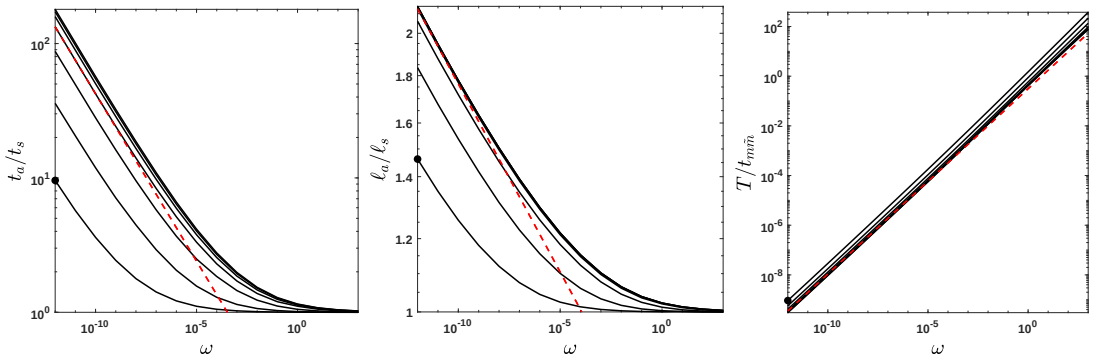

(a) $\mathrm{t_a/t_s}$ vs ω (b) ℓ_a/ℓ_s vs ω (c) $\mathsf{T}/\mathrm{t_{m\tilde{m}}}$ vs ω

Figure 5: The solid black lines indicate the numerical solutions for: (a) the arrest time to shut-in time ratios, (b) the arrest length to shut-in length ratios, and (c) the deflation time to storage-leak-off transition time ratios $\mathsf{T}/\mathrm{t_{m\tilde{m}}}$ all plotted as functions of ω for the following range of values of the regime parameter $\phi^{\mathsf{V}} = 10^{\mathsf{j}},\ \mathsf{j} \in \{-3, -2, -1, 0, 1, 2, 3\}$. In each of the figures (a)-(c) the symbol $\bullet$ plotted at the abscissa $\omega = 10^{-12}$ is used to indicate the curve corresponding to the regime parameter $\phi^{\mathsf{V}} = 10^{-3}$. In each figure, as ϕ^{V} increases the curves move progressively away from that marked with the $\bullet$ symbol. The dashed red lines represent log linear regressions for each of these plots using the first few data points for the case $\phi^{\mathsf{V}} = 1$.

The IMMA results for the non-zero toughness case are presented in figure 5, in a form similar to the $K' = 0$ results illustrated in figure 4. Here the dashed red line represents the power law $A\omega^{\alpha}$ for the particular case $\phi^V = 1$, with A and α computed by a log linear regression of the first few data points. The regression yields $\alpha = -0.25$ for t_a/t_s, consistent with the power law (46), and $\alpha = -0.041$ for ℓ_a/ℓ_s, again consistent with the power law (47).

We see that the same power law holds for all but the smallest values of ϕ^V, which would require sampling at even smaller values of ω in order for the asymptote to fully manifest itself. We observe that the t_a/t_s curves in figure 5 (a) are further spread out than those of ℓ_a/ℓ_s in figure 5 (b), because ϕ^V has a significantly larger range than $\left(\phi^V\right)^{1/6}$.

Deflation Time Scaling: In order to determine the deflation time T, we follow the same steps as for the case $K' = 0$; i.e., we match $w \sim C'\sqrt{T}$ to the aperture given in (48) and use $w_s = C' t_{m\tilde{m}}^{1/2} \omega^{1/3}$ to obtain

$$T \sim t_{m\tilde{m}} \left(\phi^V\right)^{-1/3} \omega^{3/4}. \tag{49}$$

The ratio $T/t_{m\tilde{m}}$ is plotted in figure 5 (c) as a function of the dimensionless shut-in time ω for the same range of ϕ^V values. The dashed red line represents a log linear regression of $T/t_{m\tilde{m}} \sim A\omega^{\alpha}$ using the first few data points for the case $\phi^V = 1$. The regression yields $\alpha = 0.746$, which is very close to the power law (49) predicted by the scaling analysis.

Comparing (40)-(42) to (46)-(48) and (44) to (49), we observe that expressing the scaling analysis in terms of the pair of dimensionless parameters (ω, ϕ^V) yields power laws for the arrest time, the arrest length, the arrest aperture, and the deflation time as functions of ω, which are the same for both the zero and finite fracture toughness cases.

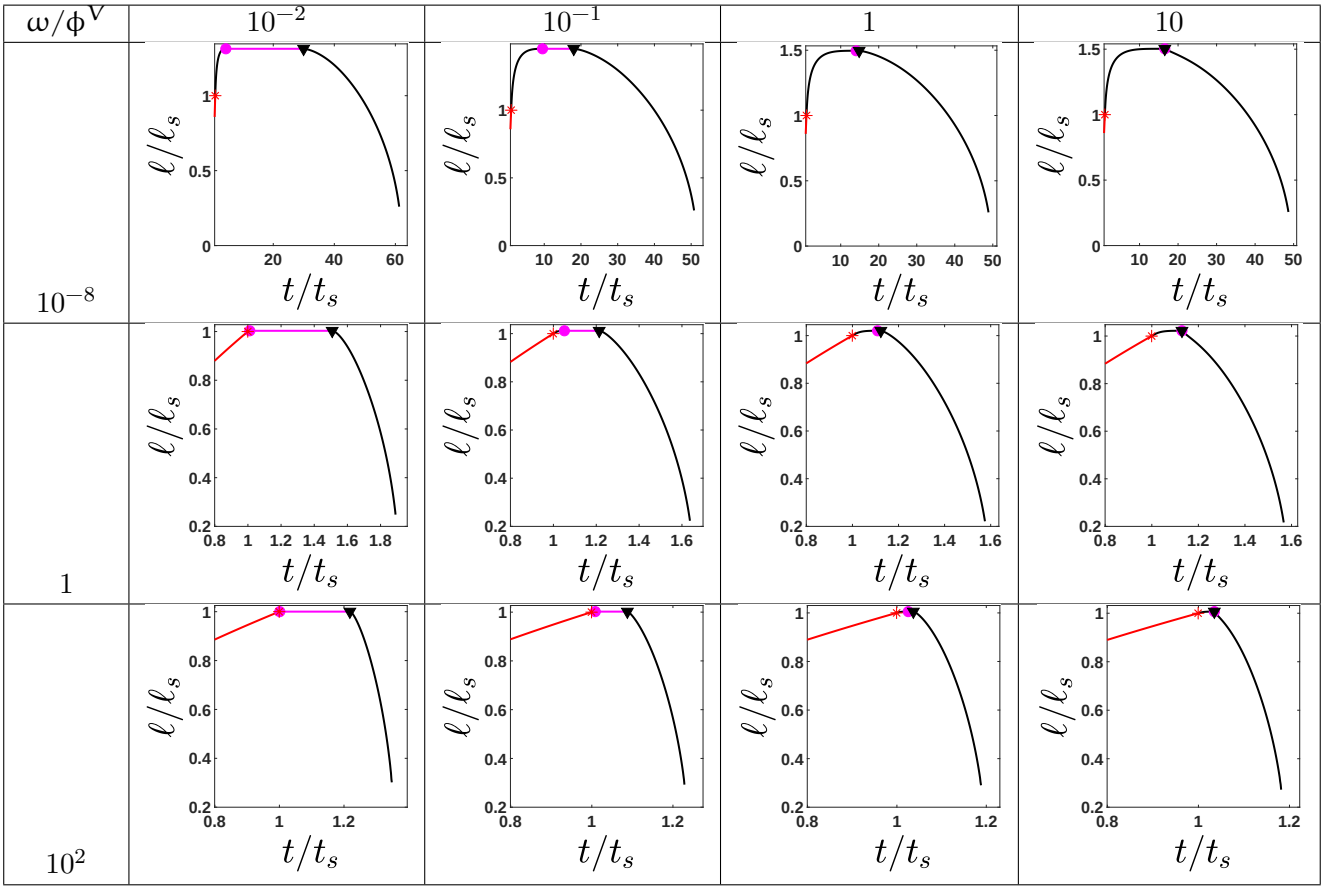

Table 1: Scaled length $\ell(t)/\ell_s$ vs t/t_s plotted for different ϕ^V and ω values

5 Receding Fracture Solution

5.1 Solution Landscape represented by the evolving fracture length ℓ

In table 1 the ratio of the fracture length scaled to the shut-in length $\ell(t)/\ell_s$ is plotted as a function of the scaled time t/t_s for a range of different ϕ^V and ω values. The value of the arrest regime parameter ϕ^V is constant for each column of the table while the value of the dimensionless shut-in parameter ω is constant for each row. Fracture lengths are plotted for $\phi^V = 10^{-2},\ 10^{-1},\ 1,\ 10$ and $\omega = 10^{-8}, 1, 10^2$. The red parts of the curve represent the dynamics up to the shut-in time t_s, which is designated by a red asterisk $*$. The subsequent black part of the curve between the red shut-in

point $*$ and the magenta arrest point $\bullet$ represents the length increase as the fracture continues to propagate between the time fluid injection ceased and the point of arrest. The magenta part of the curve between the arrest point $\bullet$ and the recession initiation point $\blacktriangledown$ represents the period during which the fracture continues to lose fluid while at arrest, so that $V = 0$ and $\frac{\partial w}{\partial t} < 0$. The subsequent black part of the curve starting with $\blacktriangledown$ represents the decreasing fracture length ℓ while the fracture recedes. Scanning down the first column $\phi^V = 10^{-2}$, we observe that the collapse time occurs a factor of 61.25 times later than the shut-in time for the case $\omega = 10^{-8}$, which is reduced to 1.89 for $\omega = 1$, and is reduced further to 1.35 for the case $\omega = 10^2$. These factors remain roughly constant for the other three columns. Scanning across the rows the proportion of the time spent deflating while arrested (magenta portions of the curves) decreases as ϕ^V is increased, while the proportion of time spent on recession alone remains almost constant. This behaviour is to be expected given the definition of ϕ^V in (34).

5.2 Aperture and Pressure profiles

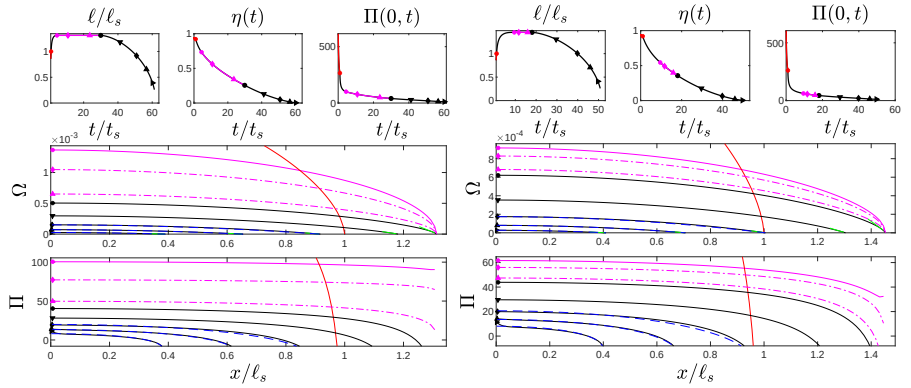

(a) $\phi^{\mathrm{V}} = 10^{-2}$ and $\omega = 10^{-8}$

(b) $\phi^{\mathrm{V}} = 10^{-1}$ and $\omega = 10^{-8}$

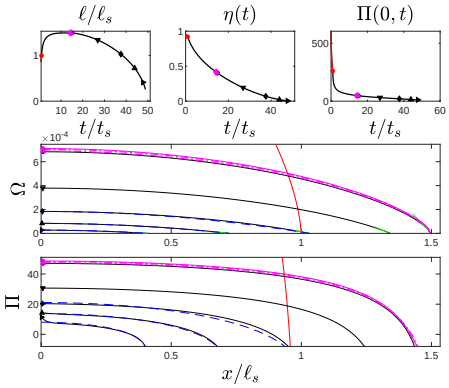

(c) $\phi^{\mathrm{V}} = 1$ and $\omega = 10^{-8}$

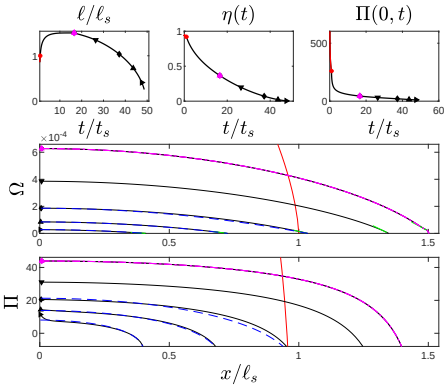

(d) $\phi^{\mathrm{V}} = 10$ and $\omega = 10^{-8}$

Figure 6: For each of (a), (b), (c), and (d) the following plots are provided: Top row: scaled fracture length ℓ/ℓ_s, fracture efficiency η, and wellbore pressure $\Pi(0,t)$ all plotted as a function of t/t_s; Middle row: snapshots of the dimensionless fracture aperture Ω after arrest (magenta and black) compared to the aperture at shut-in (red) all plotted as a function of x/ℓ_s; Bottom row: snapshots of the dimensionless pressure Π after arrest (magenta and black) compared to the pressure at shut-in (red) all plotted as a function of x/ℓ_s

In figure 6 we provide more detailed plots of the numerical solutions for the first row in table 1 associated with the value of the dimensionless shut-in time $\omega = 10^{-8}$ and the following the values of the arrest regime parameter $\phi^{\mathrm{V}} = 10^{-2},\ 10^{-1},\ 1,\ 10$ located in (a)-(d), respectively. In the first row for each parameter pair $(\phi^{\mathrm{V}}, \omega)$, we provide plots of the scaled length $\ell(t)/\ell_s$, the efficiency $\eta(t)$, and the dimensionless wellbore pressure

$\Pi(0,t)$ against the scaled time t/t_s. The efficiency is defined to be the ratio of the volume of fluid in the fracture to the pumped volume $V_f(t)$ defined below (9)

$$\eta(t) := \frac{2\int_0^{\ell} w(x,t)\,dx}{V_f(t)},$$

In the second row of each of (a), (b), (c), and (d), we provide plots of the dimensionless fracture aperture Ω against the scaled distance from the centre of the fracture x/ℓ_s for a number of sample times. The red curves represent the fracture aperture at shut-in $t = t_s$. Except for a small region near the tip, many of the red curves extend beyond the maximum ordinate range, which, for clarity, have been restricted to a maximum value set by the arrest aperture profile. The magenta curves represent the aperture profiles for the hydraulic fracture while it deflates during the arrest phase. The solid magenta curve, indicated by the magenta circle • at the wellbore, is the aperture profile sampled at the point of arrest $t = t_a$. The black curves correspond to the aperture profiles while the hydraulic fracture is receding. The curve indicated by the black circle • at the wellbore is the aperture profile sampled at the recession initiation time $t = t_r$. For the four cases considered in figure 6, the scaled sample times t/t_s that correspond to each of the symbols located at the wellbore are listed in Table 2. These symbols have also been indicated on the time evolution plots provided in the first rows of plots (a)-(d).

Subfigure	ϕ^V	•	♦	▲	•	▼	♦	▲	►
(a)	10^{-2}	4.46	10.84	23.59	29.97	41.22	50.85	56.63	60.18
(b)	10^{-1}	9.53	11.66	15.93	18.06	29.61	39.83	45.99	49.69
(c)	1	14.05	14.26	14.66	14.87	26.88	37.55	43.92	47.76
(d)	10	16.56	16.56	16.57	16.57	26.39	37.21	43.64	47.54

Table 2: The scaled sample times t/t_s corresponding to each of the markers in figure 6

As the fracture approaches the collapse time t_c it can be seen that the solutions are approximately self-similar. Indeed, it is possible to derive the following sunset similarity

solution [34] for a receding KGD fracture in a permeable elastic medium:

$$w(x,t) = g_0(t_c - t)\left(1-\xi^2\right), \; p(x,t) = \frac{(t_c-t)E' g_0}{2\pi\ell}\left[2 + \xi \log\left|\frac{1-\xi}{1+\xi}\right|\right], \; \xi = x/\ell, \; \ell = \Lambda(t_c-t)^{1/2}, \tag{50}$$

where g_0 is the constant leak-off asymptote $g = \frac{C'}{\sqrt{t-t_o(x)}} \overset{t\to t_c}{\sim} g_0$ and Λ is determined by the amount of fluid in the fracture at a given length ℓ on the way to collapse. For the last three sample times indicated by the ($\blacklozenge, \blacktriangle, \blacktriangleright$) symbols at the wellbore, the sunset solution (50) is represented by the dashed blue curves for comparison with the numerical solution. As $t \to t_c$ these two solutions show close agreement.

In the third row of each of (a), (b), (c), and (d), we provide plots of the dimensionless fracture pressure Π against the scaled distance from the centre of the fracture x/ℓ_s for a number of sample times. The red curves represent the pressure profile at shut-in $t = t_s$. Except for a small region near the tip, many of the red curves extend beyond the maximum ordinate range, which, for clarity, have been restricted to a maximum value set by the arrest pressure profile. The magenta curves represent the pressure profiles for the hydraulic fracture while it deflates during the arrest phase. The solid magenta curve, indicated by the magenta circle • at the wellbore, is the pressure profile sampled at the point of arrest $t = t_a$. The black curves correspond to the pressure profiles while the hydraulic fracture is receding. The curve indicated by the black circle • at the wellbore is the pressure profile sampled at the recession initiation time $t = t_r$. As with the aperture profiles, the scaled sample times t/t_s that correspond to each of the symbols located at the wellbore are listed in Table 2. The pressure field associated with the sunset solution is provided in (50). For the last three sample times indicated by the ($\blacklozenge, \blacktriangle, \blacktriangleright$) symbols at the wellbore, the sunset pressure profile is represented by the dashed blue curves for comparison with the numerical solution. As $t \to t_c$ there two solutions show close agreement.

5.3 Solution using field parameters

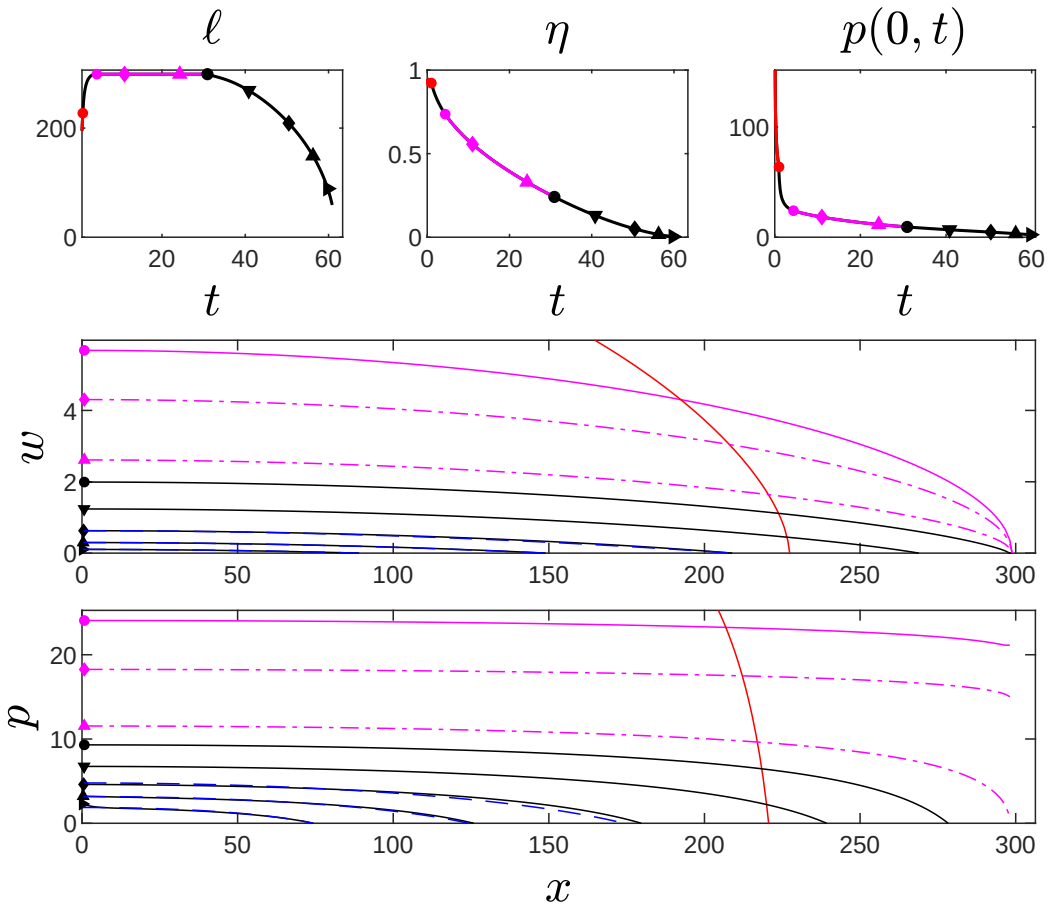

Figure 7: Top row: fracture length $\ell(t)$ [m], fracture efficiency η, and wellbore pressure $p(0,t)$ [kPa] all plotted as a function of t measured in hours [h]; Middle row: snapshots of the fracture aperture w [mm] after arrest (magenta and black) compared to the aperture at shut-in (red) all plotted as a function of x [m]; Bottom row: snapshots of the pressure p [kPa] after arrest (magenta and black) compared to the pressure at shut-in (red) all plotted as a function of x [m]

We have demonstrated that the dimensionless shut-in time ω and regime parameter ϕ^V fully characterize the arrest and recession dynamics of deflating plane strain hydraulic fractures. In order to get an idea of the range of values that the dimensionless pair (ω, ϕ^V) might assume when typical field parameters are used, consider the following ranges of material parameters: $E' \sim 1 - 30$ GPa, $\mu' \sim 10^{-2} - 10$ Pa $\cdot$ s, $C' \sim 10^{-5} - 10^{-8}$

$\mathrm{ms}^{-1/2}$, $\mathsf{K}' \sim 0.3 - 3$ MPa $\cdot\, \mathrm{m}^{1/2}$, $\mathtt{t_s} \sim 3600$ s and $\mathsf{Q}_0 \sim 10^{-5} - 10^{-3}$ $\mathrm{m}^2\mathrm{s}^{-1}$. For these ranges of material and injection parameters, the range of the dimensionless parameters is $10^{-23} \lesssim \omega \lesssim 10$ and $10^{-11} \lesssim \phi^{\mathsf{V}} \lesssim 10^4$.

We now provide a solution, in physical units and for input parameters that are within the range one might expect in the field, for a deflating KGD hydraulic fracture that arrests and recedes. Let $\mathsf{E}' = 5$ GPa, $\mu' = 0.2$ Pa $\cdot$ s, $\mathsf{C}' = 0.693 \times 10^{-5}$ $\mathrm{ms}^{-1/2}$, $\mathsf{K}' = 0.223$ MPa $\cdot\, \mathrm{m}^{1/2}$, $\mathtt{t_s} = 3600$ s and $\mathsf{Q}_0 = 10^{-3}$ $\mathrm{m}^2\mathrm{s}^{-1}$. This parameter set has been chosen so that the dimensionless shut-in time $\omega \sim 10^{-8}$ and regime parameter $\phi^{\mathsf{V}} \sim 10^{-2}$, which correspond to the case considered in figure 6 (a) in which the results were given in dimensionless form. The resemblance between the results in figure 7 and figure 6 (a) is clear. For the time evolution plots shown in the first row of figure 7 the resemblance is emphasized by the fact that $\mathtt{t}$ is plotted in hours while the shut-in time $\mathtt{t_s} = 1$ hour. Indeed, the plots are almost identical, except that the scales on the axes are now provided in physical units rather than in dimensionless form. The same symbol and line conventions have been used for figure 7 as those defined for figure 6.

6 Conclusions

In this paper we have considered the post shut-in dynamics of a deflating plane strain hydraulic fracture in a porous elastic medium. We have shown how the recently developed multiscale tip asymptotic solutions $\hat{w}_{\mathtt{kg}}$ for arrest and $\hat{w}_{\mathtt{rg}}$ for recession can be implemented in a numerical scheme that yields a smooth solution through the arrest-recession transition. In contrast, an algorithm that uses only the $\mathtt{k}$ and $\mathtt{r}$-vertex asymptotes exhibits jump discontinuities through the arrest-recession transition point, while the multiscale solution is smooth. This is because, immediately after recession starts, the linear $\mathtt{r}$-asymptote is only valid on a much smaller length scale compared to that of a tip element. Thus ascribing all the aperture in the tip to the $\mathtt{r}$-asymptote and ignoring the contribution of the $\mathtt{g}$-asymptote, results in a recession velocity that is much too large.

However, using the multiscale asymptotes, one is able to apportion these components correctly and in an adaptive fashion to achieve a smooth solution. We demonstrate that, even on a coarse mesh, the algorithm that uses the multiscale asymptotes is able to capture the power law exponents in the range $1/2 \leqslant \delta \leqslant 1$, which are predicted by asymptotic analysis. Despite the jump discontinuity through the arrest-recession transition exhibited by the algorithm using vertex as opposed to multiscale asymptotes, the two solutions ultimately converge once the transients have decayed. This analysis thus establishes the important result that, unless the purpose of the modelling is to provide a smooth solution with great detail around the arrest-recession transition point $\mathtt{t}_\mathtt{r}$, a pragmatic, and much more efficient approach, is to use a simpler algorithm based solely on vertex asymptotes.

We perform a scaling analysis using a novel parameterization in terms of the dimensionless shut-in time ω and the dimensionless arrest regime parameter ϕ^V, which are able to capture the power law dependencies on ω of the arrest time, the arrest length, the arrest aperture, and the deflation time, which remain the same for both the zero and finite fracture toughness cases. All these power law relationships are confirmed using a numerical scheme that uses the arrest-recession multiscale tip solutions, which were established using rigorous asymptotic analysis.

Using an implicit moving mesh algorithm that incorporates the rigorous multiscale arrest-recession asymptotics, we explore the impact that changes in the dimensionless parameters ω and ϕ^V have on the time between shut-in and arrest, the duration of arrest, and the elapsed time from the initiation of arrest to collapse of the fracture. For fixed ϕ^V, the ratio $\mathtt{t}_\mathtt{c}/\mathtt{t}_\mathtt{s}$ between the collapse time and the shut-in time decreases as the dimensionless shut-in time ω increases. For fixed ω, the proportion of time spent deflating while the fracture has arrested decreases as ϕ^V increases, while the proportion of time spent solely on recession remains almost constant. We discuss the range of values that the pair (ω, ϕ^V) are likely to assume if the injection rate and material parameters

are restricted to values one might expect in the field. We also provide, for a value of the pair $(\omega, \phi^{\mathsf{V}})$ that might occur in the field, the post shut-in solution in physical units for a plane strain hydraulic fracture that propagates after shut-in, deflates during arrest, and recedes till collapse.

Acknowledgments

AP was supported by the Natural Sciences and Engineering Research Council of Canada (NSERC) (grant number RGPIN-2015-06039) and the British Columbia Oil and Gas Commission. ED gratefully acknowledges support provided by the T.W. Bennett Chair in Mining Engineering and Rock Mechanics.

References

[1] Adachi, J., Siebrits, E., Peirce, A. and Desroches, J. 2007 Computer Simulation of Hydraulic Fractures. *Int. J. Rock Mech. & Min. Sci.*, **44**, pp. 739-757.

[2] Adachi J.I. and Detournay E. 2008 Plane-strain propagation of a fluid-driven fracture in a permeable medium, *Engrg. Fract. Mech.* **75**, pp. 4666-4694.

[3] Adachi J.I. , Detournay E., and Peirce, A. 2010 An Analysis of Classical Pseudo-3D Model for Hydraulic Fracture with Equilibrium Height Growth across Stress Barriers, *Int. J. Rock Mech. & Min. Sci.*, **47**, pp. 625-639.

[4] Bunger A.P., Detournay E. 2008. Experimental validation of the tip asymptotics for a fluid-driven crack. *J. Mech. Phys. Solids*, **56** pp.3101â15.

[5] Carter, E.D. 1957 Optimum fluid characteristics for fracture extension, in: G.C. Howard, C.R. Fast (Eds.), *Drilling and Production Practices* , American Petroleum Institute, Tulsa, OK, pp. 261-270.

[6] De Pater, H., Desroches, J., Groenenboom, J., and Weijers, L. 1996 Physical and numerical modelling of hydraulic fracture closure. *SPE Production Facilities*, **11** (02) pp. 122â128.

[7] Desroches,J., Detournay,E., Lenoach,B., Papanastasiou,P., Pearson, J.R.A.,Thiercelin,M., and Cheng, A.H.D. 1994 The Crack Tip Region in Hydraulic Fracturing, *Proc. R. Soc. London*, Ser.A, **447**, pp.39â48.

[8] Desroches, J. and Thiercelin, M. 1993 Modelling the propagation and closure of microhydraulic fractures. *Int. J. Rock Mech. & Min. Sci.*, **30**(7) pp. 1231â1234.

[9] Detournay E. 2004 Propagation regimes of fluid-driven fractures in impermeable rocks , *Int. J. Geomech.*, **4** (1), pp. 1â11.

[10] Detournay E. 2016, Mechanics of Hydraulic Fractures, *Annu. Rev. Fluid Mech.* **48** pp. 311-39.

[11] Detournay E. and Peirce A. 2014 On the Moving Boundary Conditions for a Hydraulic Fracture, *Int. J. Eng. Sci.* ,**84**, pp. 147-155.

[12] Dontsov, E., Peirce, A., 2015 An enhanced pseudo-3D model for hydraulic fracturing accounting for viscous height growth, non-local elasticity, and lateral toughness, *Engrg. Fract. Mech.*, **42**, pp. 116-139.

[13] Dontsov E.V. 2016 An approximate solution for a penny-shaped hydraulic fracture that accounts for fracture toughness, fluid viscosity and leak-off. *R. Soc. open sci.* **3** pp. 160737.

[14] Dontsov E.V. 2017 An approximate solution for a plane strain hydraulic fracture that accounts for fracture toughness, fluid viscosity, and leak-off, *Int. J. Fract.* **205** pp. 221-237.

[15] Dontsov, E. and Peirce, A. 2015 A non-singular integral equation formulation to analyse multiscale behaviour in semi-infnite hydraulic fractures, *J. Fluid Mech. (JFM RAPIDS)*, **781**, R1.

[16] Dontsov E.V. and Peirce, A. 2017 A multiscale Implicit Level Set Algorithm (ILSA) to model hydraulic fracture propagation incorporating combined viscous, toughness, and leak-off asymptotics, *Comp. Meth. in Appl. Mech. and Eng.*, **313** pp. 53-84.

[17] Garagash D.I. and Detournay E. 2000 The tip region of a fluid-friven fracture in an elastic medium, *ASME J. Appl. Mech.*, **67**, (1) pp. 183-192.

[18] Garagash D.I. 2006 Plane-strain propagation of a fluid-driven fracture during injection and shut-in: Asymptotics of large toughness, *Engrg. Fract. Mech.*, **73**, pp. 456-481.

[19] Garagash, D. I., Detournay, E., and Adachi, J. I. 2011 Multiscale tip asymptotics in hydraulic fracture with leak-off. *J. Fluid Mech.*, **669** pp. 260-297.

[20] Hills D.A., Kelly P.A., Dai D.N. and Korsunsky A.M. 1996, *Solution of crack problems, The Distributed Dislocation Technique, Solid Mechanics and its Applications*, vol.44, Kluwer Academic Publisher, Dordrecht.

[21] Mohammadnejad, T. and Andrade, J. E. 2016 Numerical modelling of hydraulic fracture propagation, closure and reopening using XFEM with application to in-situ stress estimation, *Int. J. Numer. Anal. Meth. Geomech.*, **40** (15) pp. 2033â2060.

[22] Economides, M. J. and Nolte, K. G. 2000 *Reservoir Stimulation*, John Wiley Sons.

[23] Khristianovic, S.A. and Zheltov Y.P. 1955 Formation of vertical fractures by means of highly viscous fluids, in: *Proc. 4th World Petroleum Congress*, **vol. 2**, pp. 579â586.

[24] Lecampion B., Peirce A., Detournay E., Zhang X., Chen Z., Bunger A., Detournay C., Napier J., Abbas S. , Garagash D., and Cundall P. 2013, The impact of the near-tip logic on the accuracy and convergence rate of hydraulic fracture simulators compared to reference solutions, Chapter 43, *Effective and Sustainable Hydraulic Fracturing* , InTech, ISBN 978-953-51-1137-5, doi:10.5772/45724, pp. 1000.

[25] Lister J. 1990 Buoyancy-driven fluid fracture: The effects of material toughness and of low-viscosity precursors. *J. Fluid Mech.*, **210** pp. 263â280.

[26] Madyarova, M. 2003 Fluid-Driven Penny-Shaped Fracture in Permeable Rock, M.Sc. Thesis, University of Minnesota.

[27] McClure, M. W. and Horne, R. N. 2013 *Discrete Fracture Network modelling of Hydraulic Stimulation: Coupling Flow and Geomechanics*, SpringerBriefs in Earth-Sciences, Springer.

[28] Mori A. and Lecampion B. 2021 Arrest of a radial hydraulic fracture upon shut-in of the injection, *Int. J. Solids Struct.* **219â220** pp. 120â133.

[29] Nolte, K. G. 1979 Determination of fracture parameters from fracturing pressure decline. *In Proc. SPE Ann. Tech. Conf. & Exhib., Las Vegas* SPE 8341.

[30] Peirce, A. and Detournay, E. 2008 An Implicit Level Set Method for modelling Hydraulically Driven Fractures, *Comp. Meth. in Appl. Mech. and Eng.*, **197** pp. 2858-2885.

[31] Peirce, A. 2015 modelling multi-scale processes in hydraulic fracture propagation using the implicit level set algorithm, *Comp. Meth. in Appl. Mech. and Eng.*, **283** pp. 881-908.

[32] Peirce, A. 2016 Implicit level set algorithms for modelling hydraulic fracture propagation, *Phil. Trans. R. Soc. A* **374** pp. 20150423.

[33] Peirce, A. and Detournay, E. 2022 Multiscale tip symptotics for a deflating hydraulic fracture with leak-off, *J. Fluid Mech.*, **Vol 947**, **A17**, (doi:10.1017/jfm.2022.623).

[34] Peirce, A. and Detournay, E. 2022 Sunset Similarity Solution for a Receding Hydraulic Fracture, *J. Fluid Mech.*, **Vol 944**, **A7**, (doi:10.1017/jfm.2022.430).

[35] Peirce, A. 2022 The Arrest and Recession Dynamics of a Deflating Radial Hydraulic Fracture in a Permeable Elastic Medium, *J. Mech. Phys. Solids*, **166**, pp. 104926, (doi.org/10.1016/j.jmps.2022.104926).

[36] Rice, J. R. 1968 *Mathematical Analysis in the Mechanics of Fracture, Fracture, an Advanced Treatise*, H. Liebowitz, ed. Academic Press, New York, Chap. 3, pp. 191-311.

[37] Savitski A. and Detournay E. 2002 Propagation of a fluid-driven penny-shaped fracture in an impermeable rock: asymptotic solutions. *Int. J. Solids Struct.* **39** pp. 6311-6337.

[38] Spence,D.A. and Sharp,P. 1985 Self-similar solutions for elastohydrodynamic cavity flow, *Proc. R. Soc. London*, Ser.A, **400**, pp. 289-313.

[39] van Dam, D. B., de Pater, C. J., and Romijn, R. (2000). Analysis of hydraulic fracture closure in laboratory experiments. *SPE Production & Facilities*, **15** (03) pp. 151â158.

[40] Zanganeh, B., Clarkson, C. R., and Hawkes, R. V. 2017 Reinterpretation of fracture closure dynamics during diagnostic fracture injection tests, *In Proc. SPE Ann. Tech. Conf. & Exhib., The Woodlands, Texas*, SPE-189840-MS.